INTERNATIONAL JOURNAL FOR NUMERICAL METHODS IN FLUIDS
Int. J. Numer. Meth. Fluids 2008; **56**:185–208

Dynamic stall modelling on airfoils based on strong viscous–inviscid interaction coupling

Vasilis A. Riziotis*,† and Spyros G. Voutsinas

Fluids Department, School of Mechanical Engineering, National Technical University of Athens,
9 Heroon Polytechneiou, GR15780, Athens, Greece

SUMMARY

The prediction of the aerodynamic performance of pitching airfoils in stall conditions is considered in the context of strong viscous–inviscid interaction modelling. The aim of the work is to demonstrate the capabilities of a low-cost dynamic stall model well suited for engineering applications. The model is formulated on the basis of a standard panel method combined with a vortex blob approximation of the wake. The development of the boundary layer over the airfoil and the evolution of the shear layer in the wake are taken into account by means of strong viscous–inviscid interaction coupling. To this end a transpiration layer is added to the inviscid formulation which represents the displacement effect viscosity results in the flow while the non-linear coupled equations are solved simultaneously. Separation is modelled by introducing a second wake originating from the separation point ('double-wake' concept) which is provided as part of the boundary layer solution. The theoretical presentation of the model is supported with favourable comparisons to four sets of wind tunnel measurements. Copyright © 2007 John Wiley & Sons, Ltd.

Received 3 October 2006; Revised 10 April 2007; Accepted 15 April 2007

KEY WORDS: dynamic stall; boundary layer methods; panel methods; viscous–inviscid interaction

1. INTRODUCTION

Dynamic stall is of particular interest to rotor aerodynamics. It is closely connected to the aerodynamic performance of rotors while it is critical in vibration analysis and aeroelastic stability. For helicopter rotors dynamic stall will appear over the retreating side as a result of the pitch control. The development of stall in combination with the relatively high reduced frequencies characterizing the oscillatory motion of helicopter blades can lead to significantly increased vibratory loads. In wind energy applications, the understanding and quantitative analysis of dynamic stall is vital.

---

*Correspondence to: Vasilis A. Riziotis, Fluids Department, School of Mechanical Engineering, National Technical University of Athens, 9 Heroon Polytechneiou, GR15780, Athens, Greece.

†E-mail: vasilis@fluid.mech.ntua.gr

Stall-regulated and active stall wind turbines will operate in dynamic stall conditions during a substantial part of their lifetime while pitch-regulated machines will inevitably encounter dynamic stall around rated wind conditions.

Our present understanding on the underlying mechanisms is still insufficient [1]. In many aspects we lack fundamental knowledge on flows at high Reynolds numbers, which are of direct relevance with regard to the occurrence and evolution of stall. For example, it is still unclear even in the case of a pitching airfoil, how the reduced frequency and the Reynolds number affect the unsteady loading of the airfoil.

On the modelling level, the prediction of dynamic stall is still largely based on empiricism at least in practice. The dynamic stall models in most comprehensive codes use steady 2D lift and drag characteristics and then introduce time-dependent variations based on either time delay schemes or on a set of dynamic equations properly calibrated with measurements [2, 3]. The main advantage of these models is that they are fully compatible with blade element and lifting line theories and cost nearly nothing in terms of CPU time. So, they are well suited for time domain aeroelastic calculations, which is the ultimate objective of rotor analysis. Experimental evidence as well as numerical results, however, indicate that engineering models can be incorrect, especially in predicting deep stall. Considerable effort has been put during the last years on the calibration of different empirical dynamic stall models aiming at accomplishing better predictions [4, 5]. In parallel, continuous work is carried out on RANS models aiming at a deeper understanding of the underlying mechanisms. RANS models, however, are still too expensive to be included in any kind of aeroelastic calculations of realistic rotor systems. Furthermore especially in terms of transition and turbulence modelling several open issues remain [6]. So, although the refinement of RANS models is indispensable, non-empirical models of low computational cost are still needed. Aiming at low computational cost, the present work proposes an intermediate path based on vortex methods.

Vortex methods constitute a distinct class of numerical approximations in fluid mechanics. They are grid free; they use as building blocks elementary flows, namely flows generated by properly regularized point vortices; they solve the flow equations in material coordinates and therefore they can naturally adopt to local conditions; they are relatively easy to implement and parallelize; in case viscous effects are neglected as in classical aerodynamic theory, vortex methods are also very efficient. The interest in vortex methods has been renewed in the early 1980s when their rigorous mathematical analysis was first accomplished [7, 8]. Since then vortex and more generally particle methods progressed a lot [9]. In many aspects they can be considered as an alternative method in computational fluid dynamics (CFD). However when used in simulating viscous flows some of their nice features are lost. In particular, the fulfilment of the no slip condition on solid boundaries requires the generation of a large number of vortices and consequently the cost increases and becomes comparable to the cost of conventional CFD methods [9]. Furthermore for turbulent flows, turbulence closure is not straightforward. All turbulence closure models have been developed with reference to the velocity–pressure formulation of the flow equations and not the vorticity–velocity formulation on which vortex methods rely. So aiming at a cost-effective model that can stand in between detailed CFD and empirical modelling, the simplest possible option of vortex method should be used.

Previous experience with dynamic stall modelling on pitching airfoils has shown that vortex methods need not model viscous effects in detail in order to give good load predictions [10]. This fits well with the objective of a low-cost model. The velocity field for an arbitrarily moving airfoil is defined through source and vorticity distributions defined on the surface of the airfoil and vortex blobs in the wake. For attached flow conditions, this corresponds exactly to the model of Basu and Hancock [11]. In the same context it is possible to extend vortex modelling to separated flows [12–15] by introducing in addition to the trailing edge vortex sheet a second sheet originating from the separation point. This double-wake formulation is based on the remark that at separation, vorticity is continuously released in the free flow along a strong shear layer that forms the separation bubble. When the location of separation is provided externally, it has been proved [16] that a purely inviscid calculation can give quite good load predictions. This happens because the wake vorticity provides enough feedback to the pressure field over the airfoil. There is an obvious deficiency in this approach: the location of separation is an external input which we normally do not have. Because separation is a purely viscous process, the double-wake model must be supplemented with a separation prediction model. To this end, thin boundary layer theory is applied.

Thin boundary layer theories and in particular their integral formulations underwent their peak development in the seventies and early eighties. Numerous models have been developed, each trying to give as accurate as possible predictions. The literature is extremely extensive, so only some of the most important references are quoted [17–21]. A recent survey of the various methods can be found in [1]. Among the different models, those of LeBalleur [20] and Drela [17] proved to be most successful in simulating separated flows. Comparing the two models is difficult. LeBalleur succeeded in converging at deeper stall than Drela. However, Drela's approach is simpler to implement and better suited to panel methods and for this reason has been chosen in the present work. In fact, the proposed model can be regarded as an extension of Drela's model to cases of dynamic stall. It is noted that the formulation considered concerns incompressible flows and therefore it is applicable to wind turbines.

The paper is organized as follows. In Section 2, the formulation of the model is described. First the integral relations of potential flows are reviewed. Then the inviscid vortex model is described. Next the viscous part is presented in brief, followed by the description of the viscous–inviscid coupling procedure. In Section 3 results from steady and unsteady calculations are presented and discussed in comparison with measurements. It is concluded that at its present state the model is stand alone predictive and reliable tool in providing satisfactory results even in cases where massive separation occurs.

2. FORMULATION OF THE MODEL

Viscous–inviscid interaction integral models are based on the assumption that it is possible to define an 'equivalent inviscid flow (EIF)'

$$\mathbf{u}_e = \mathbf{u}^0 + \mathbf{u}^* \tag{1}$$

capable of incorporating the main effects of the real flow. For the flow around an airfoil such an assumption is approximately valid at high *Re* numbers. The boundary layer and the shear layer in the wake are expected to be thin and therefore it is possible to approximate their effect on the flow by means of properly defined singularity distributions. For an incompressible flow, the solid surface and the line representing the wake will be the active boundaries on which source and vorticity surface distributions are defined in order to simulate the effect of the associated boundary and shear layers. However, in the particular case the flow separates, the wake is no longer thin. This inconsistency is overcome by introducing two distinct thin shear layers, one originating from

DOI: 10.1002/fld

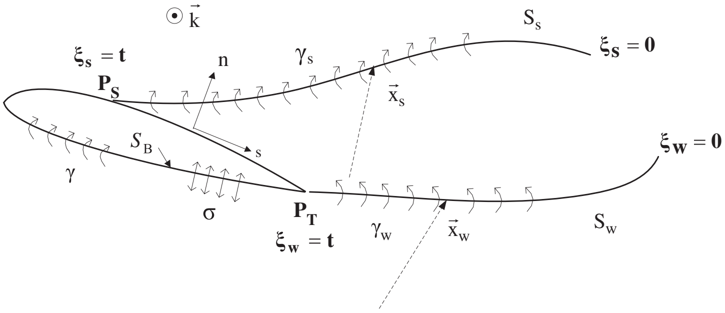

Figure 1. Singularity distributions on the airfoil and the wakes.

the trailing edge of the airfoil and the other from the separation point (Figure 1). These two points are the locations where the airfoil releases (emits) vorticity into the free flow. If during the cyclic motion of the airfoil, the flow conditions bring the flow to full reattachment then the two layers will collapse at the trailing edge into one single shear layer.

2.1. *Integral representation of potential flows*

For a potential flow vanishing at infinity and continuous everywhere except on a finite number of lines (in the present case the airfoil surface and the two shear layers in the wake), Green's theorem leads to the following integral representation:

$$\mathbf{u}(\mathbf{x};t) = \frac{1}{2\pi}\int_{S_B+S_W+S_S} ([u_n](\mathbf{y};t) - [u_\tau](\mathbf{y};t)\mathbf{k}\times)\frac{\mathbf{r}}{r^2}\,\mathrm{d}s(\mathbf{y}) \tag{2}$$

In (2), $[u_n]$ is identified to a source distribution σ, whereas $[u_\tau]$ to surface vorticity γ. σ on S_B is associated to the no-penetration condition on S_B while on $S_W + S_S$, σ will vanish. γ is defined everywhere on $S_B+S_W+S_S$ and is determined by the Kutta condition at the emission points together with Kelvin's theorem. The above interpretation of (2) corresponds to an indirect formulation. By assuming the flow within the airfoil stagnant, a direct formulation can be obtained in which on S_B, $[u_n]=\mathbf{u}\cdot\mathbf{n}=u_n$ is known directly from the boundary condition while $[u_\tau]=\mathbf{u}\cdot\boldsymbol{\tau}=u_\tau$ is determined by satisfying (2) on S_B [22].

2.2. *The representation of* $\mathbf{u}^0$

For $\mathbf{u}^0$, the indirect formulation is used. Taking piecewise constant approximations for both σ and γ, for attached flows [10, 11], $\mathbf{u}^0$ will be defined by the source strengths on S_B $\{\sigma^i, i=1:N\}$, one for each segment, and a uniform vorticity distribution γ^1. On S_W, γ_W is integrated on each wake segment except for that in contact with the airfoil at the trailing edge, leading at $t=m\cdot\Delta t$ to a vortex blob approximation defined by $\{\Gamma_W^j, \mathbf{Z}_W^j, j=1:m-1\}$ plus a vortex segment ΔS_W^Δ with intensity γ_W^Δ and orientation θ_W^Δ (Figure 2(a)). With the onset of separation, a second wake S_S is introduced also defined by a collection of vortex blobs $\{\Gamma_S^j, \mathbf{Z}_S^j, j=1:m-1\}$ plus a vortex segment ΔS_S^Δ with intensity γ_S^Δ and orientation θ_S^Δ. In addition to the second wake, the bound vorticity definition changes to a two value function: γ^1 is the uniform vorticity over the attached

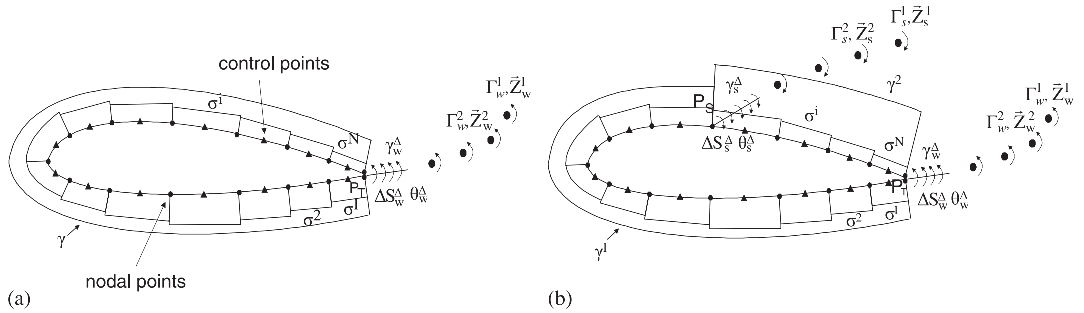

Figure 2. D.o.f. of the potential problem.

part (i.e. up to segment $N_{P_s}-1$) while over the separated part a different uniform value γ^2 is assumed (Figure 2(b)). Note that P_s can change in time. So,

$$\begin{aligned}\mathbf{u}^0(\mathbf{x};t) &= \mathbf{U}_\infty + \sum_{i=1}^{N}\frac{\sigma^i(t)}{2\pi}\int_{S_B^i}\frac{\mathbf{r}}{r^2}\,\mathrm{d}s(\mathbf{y}) + \frac{\gamma^1(t)}{2\pi}\sum_{i=1}^{N_{P_s}-1}\int_{S_B^i}\frac{\mathbf{r}\times\mathbf{k}}{r^2}\,\mathrm{d}s(\mathbf{y})\\ &\quad + \frac{\gamma^2(t)}{2\pi}\sum_{i=N_{P_s}}^{N}\int_{S_B^i}\frac{\mathbf{r}\times\mathbf{k}}{r^2}\,\mathrm{d}s(\mathbf{y}) + \sum_{p=w,s}\frac{\gamma_p^\Delta(t)}{2\pi}\int_{\Delta S_p^\Delta(t)}\frac{\mathbf{r}\times\mathbf{k}}{r^2}\,\mathrm{d}s(\mathbf{y})\\ &\quad + \sum_{\substack{j=1\\ p=w,s}}^{m-1}\frac{\Gamma_p^j}{2\pi}\frac{(\mathbf{x}-\mathbf{Z}_p^j(t))\times\mathbf{k}}{|\mathbf{x}-\mathbf{Z}_p^j(t)|^2}\end{aligned} \tag{3}$$

The source intensities are associated with the no-penetration condition:

$$(\mathbf{u}^0(\mathbf{x};t)-\mathbf{U}_B(\mathbf{x};t))\cdot\mathbf{n}(\mathbf{x};t) = \mathbf{w}^0(\mathbf{x};t)\cdot\mathbf{n}(\mathbf{x};t) = 0 \tag{4}$$

while the remaining vorticity unknowns are determined by the emission conditions as follows. The separation region located between the two wakes S_W and S_S is assumed isolated from the rest of the flow. So there will be a pressure difference Δh with respect to the outer region. Then by applying Bernoulli's equation at the two sides of each wake it follows that for zero pressure jump:

$$-\left[\frac{w^2}{2}\right]_W = \frac{\partial}{\partial t}[\Phi]_W + \Delta h, \quad \left[\frac{w^2}{2}\right]_S = -\frac{\partial}{\partial t}[\Phi]_S + \Delta h \tag{5}$$

Combining the two and noting that the airfoil circulation $\Gamma = \gamma^1 L_1 + \gamma^2 L_2 = [\Phi]_W + [\Phi]_S$,

$$-\frac{\partial\Gamma}{\partial t} = \left[\frac{w^2}{2}\right]_W + \left[\frac{w^2}{2}\right]_S \cong [w_\tau]_W\underbrace{\frac{(w_\tau)_W^+ + (w_\tau)_W^-}{2}}_{(\overline{w}_\tau)_W} + [w_\tau]_S\underbrace{\frac{(w_\tau)_S^+ + (w_\tau)_S^-}{2}}_{(\overline{w}_\tau)_S} \tag{6}$$

The above equation is equivalent to Kelvin's theorem if the emission velocity is taken equal to the mean velocity calculated on the airfoil at the two sides with respect to the emission point

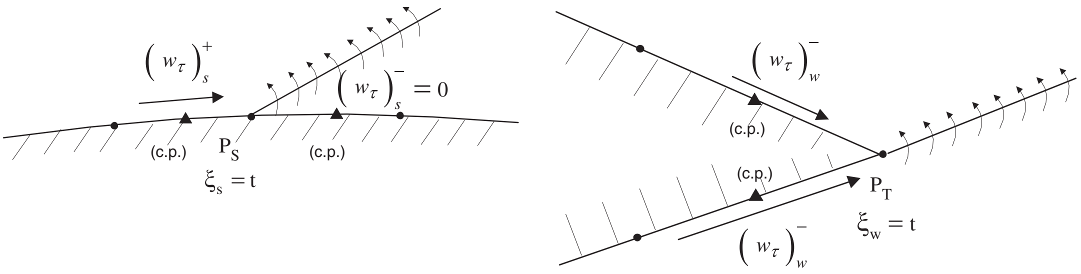

Figure 3. Application of Kutta condition at the trailing edge and the separation point.

(Figure 3):

$$\Delta S_W^\Delta = (\overline{w}_\tau)_W \cdot \Delta t, \quad \Delta S_S^\Delta = (\overline{w}_\tau)_S \Delta t \tag{7}$$

and that the velocity jump gives the rate at which vorticity is released:

$$\gamma_W|_{P_T} = [w_\tau]_W, \quad \gamma_S|_{P_S} = [w_\tau]_S \tag{8}$$

Note that the above analysis holds for $\mathbf{w}^0$ as well as $\mathbf{w}_e$.

In summary (6) provides an equation for the bound circulation Γ, (7) determines the lengths of ΔS_W^Δ and ΔS_S^Δ, whereas (8) give the emitted vorticities. In order to close the system of equations, an extra condition at the segment just after separation is added, requiring that the velocity at the N_{P_s} control point is zero. Finally as regards the orientation of emission, it is assumed that at the trailing edge the wake segment will be aligned to the lower or upper side of the airfoil depending on whether the sign of change in the bound circulation while at the separation point the direction is determined by averaging the velocity at the segment centres adjacent to the separation point.

There is a continuous process of releasing vorticity which will gradually generate the wakes as material lines carrying surface vorticity. Their evolution in time is subjected to convection defined by the mean velocity at any point of S_W or S_S, while the vorticity intensities Γ_p^j are conserved.

2.3. The viscous layers

In formulating the viscous part of the problem, the two equations model defined by Drela [18] is closely followed; therefore, the presentation is restricted only to what was added to account for the unsteadiness of the flow and the treatment of separation. For both the boundary and wake shear layers of the real viscous flow, the thin approximation of the unsteady momentum and kinetic energy deficit equations are introduced in integral form for the EIF velocity $\mathbf{w}_e$ (the underlined terms denote the unsteady terms):

$$\underline{\frac{1}{\rho_e w_{e\tau}^2}\frac{\mathrm{d}}{\mathrm{d}t}(\rho_e w_{e\tau}\delta^*)} + \frac{\mathrm{d}\theta}{\mathrm{d}s} + (2+H)\frac{\theta}{w_{e\tau}}\frac{\mathrm{d}w_{e\tau}}{\mathrm{d}s} + \frac{\theta}{\rho_e}\frac{\mathrm{d}\rho_e}{\mathrm{d}s} = \frac{C_f}{2} \tag{9}$$

$$\begin{gathered}\underline{\frac{1}{\rho_e w_{e\tau}^3}\frac{\mathrm{d}}{\mathrm{d}t}(\rho_e w_{e\tau}^2\theta)+\frac{1}{\rho_e w_{e\tau}}\frac{\mathrm{d}}{\mathrm{d}t}(\rho_e\delta^*)+\frac{2}{w_{e\tau}^2}\frac{\mathrm{d}w_{e\tau}}{\mathrm{d}t}H^{**}\theta-\frac{H^*}{\rho_e w_{e\tau}^2}\frac{\mathrm{d}}{\mathrm{d}t}(\rho_e w_{e\tau}\delta^*)} \\ \underline{-\frac{4\Omega}{w_{e\tau}}\Theta_n}+\theta\frac{\mathrm{d}H^*}{\mathrm{d}s}+(2H^{**}+H^*(1-H))\frac{\theta}{w_{e\tau}}\frac{\mathrm{d}w_{e\tau}}{\mathrm{d}s}=2C_D+\underline{\frac{2a}{w_e^2}\delta^*}-H^*\frac{C_f}{2}\end{gathered} \tag{10}$$

The above set is completed with a closure equation and closed-form empirical expressions for all boundary layer parameters which relate them to δ^* and θ, the local flow conditions as expressed by the local Mach number Ma_e and the local momentum thickness Reynolds number Re_θ [23]. Over the laminar part of the boundary layer, the closure equation consists of a transition prediction model based on the e^N spatial amplification theory [24], whereas over the turbulent part corresponds to a dissipation closure equation for the maximum shear stress coefficient C_τ [25, 26]. The empirical expressions although suitable for flows with extended trailing edge separation have been developed for steady turbulent flows and are not corrected for unsteady flow effects. Therefore, they can only be used on the condition that relatively slow unsteady flows are considered.

The d.o.f. of the boundary layer equations are taken at the panel centres and two-point central difference schemes are used for discretization. There are three unknowns at each element centre, namely the displacement thickness δ^{*i}, the momentum thickness θ^i, the amplification factor η^i (provided by the transition equation in the laminar part) or the shear stress coefficient C_τ^i (provided by the stress transport equation in the turbulent part) through which C_D is determined [17].

2.4. *The viscous–inviscid coupling*

Standard in integral boundary layer theory is the definition of the transpiration velocity:

$$[u_n^*]_B=w_{e,n}|_{\text{wall}}=\frac{\mathrm{d}}{\rho_e\,\mathrm{d}s}(\rho_e w_{e,\tau}\delta^*)\equiv\frac{\mathrm{d}M_B}{\mathrm{d}s} \tag{11}$$

as the means of viscous–inviscid coupling. For an inviscid flow,

$$M_B=w_{e\tau}\delta^* \tag{12}$$

defines the volume flux corresponding to the deficit of the real flow with respect to the EIF. In particular, (11) defines a Neumann condition (or equivalently an extra source distribution) for $\mathbf{u}^*$ through which the viscous and inviscid parts of $\mathbf{u}_e$ are coupled. The extra sources correspond to the transpiration on both the boundary and the shear layers. The realization, however, depends on the number of wakes introduced in the inviscid part. Two different models have been formulated as presented next.

2.4.1. The single-wake model. For attached but also for moderately separated flows, it is possible to only retain the trailing edge wake as in [17]. In this case the two boundary layer equations (9) and (10) together with the supplementary equations for the transition disturbance amplification factor η and the shear stress coefficient C_τ are solved starting from the stagnation point near the leading edge and moving towards the trailing edge along the two sides of the airfoil, as shown in Figure 4(a). Along the trailing edge wake the boundary layer equations are satisfied on both sides of the free shear layer (upper and lower) assuming zero friction ($C_f=0$). For this purpose a wake panelling is introduced which extends a few chord lengths downstream the trailing edge. When (11) is applied to the two sides of the wake, the jump of the normal to S_W velocity

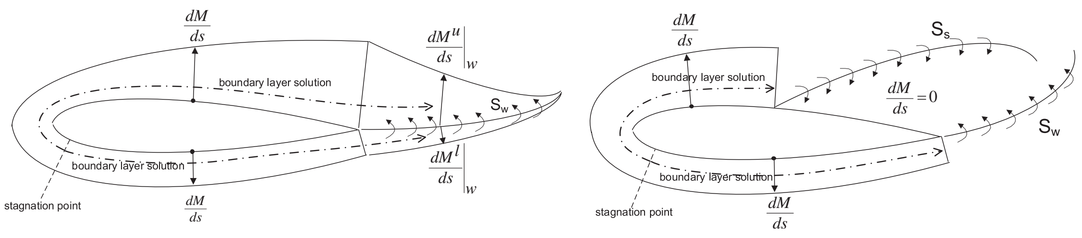

single wake double wake

Figure 4. Transpiration velocity distribution along the airfoil and the wakes.

is obtained:

$$[u_n^*]_W = (w_{e,n}^u - w_{e,n}^\ell)_W = \frac{\mathrm{d}}{\rho_e\,\mathrm{d}s}(\rho_e w_{e,\tau}\delta^*)_W^u + \frac{\mathrm{d}}{\rho_e\,\mathrm{d}s}(\rho_e w_{e,\tau}\delta^*)_W^\ell \cong \frac{\mathrm{d}M_W^u}{\mathrm{d}s} + \frac{\mathrm{d}M_W^\ell}{\mathrm{d}s} \tag{13}$$

By introducing $[u_n^*]_B$ and $[u_n^*]_W$ in (2), based on (11) and (13) and assuming $[u_\tau^*]_W = 0$, the direct integral representation of $\mathbf{u}^*$ is obtained on S_B. It provides an integral equation for the tangential viscous correction velocity $u_{\tau B}^*$. The solution will be a function of the volume fluxes M on S_B and S_W realizing the viscous–inviscid coupling. At the discrete level, the form of (11) and (13) suggests to use piecewise linear interpolation for $[u_n^*]_B$ and $[u_n^*]_W$. Using standard finite difference formulas, the nodal values of $[u_n^*]_B$ and $[u_n^*]_W$ are obtained:

$$[u_n^*]_{B,I} = \sum_{i=1}^{N} D_{I,i} M_B^i, \quad [u_n^*]_{W,I} = \sum_{i=1}^{N_w} D_{I,i}(M_W^u + M_W^\ell)^i \tag{14}$$

where $D_{I,i}$ denotes the operator correlating the M^i flux with the normal velocity correction at grid node I. Unlike $[u_n^*]_B$ and $[u_n^*]_W$, $u_{\tau B}^*$ is approximated as piecewise constant distribution. Therefore,

$$\begin{aligned}\mathbf{u}^*(\mathbf{x};t) = {} & \sum_{i=1}^{N} \frac{(u_{\tau B}^*)_i}{2\pi} \int_{S_B^i} \frac{\mathbf{r}\times\mathbf{k}}{r^2}\,\mathrm{d}s(\mathbf{y}) + \sum_{i=1}^{N} \int_{S_B^i} \frac{[u_n^*]_B(\mathbf{y})}{2\pi}\frac{\mathbf{r}}{r^2}\,\mathrm{d}s(\mathbf{y}) \\ & + \sum_{i=1}^{N_w} \int_{\Delta S_w^i} \frac{[u_n^*]_W(\mathbf{y})}{2\pi}\frac{\mathbf{r}}{r^2}\,\mathrm{d}s(\mathbf{y})\end{aligned} \tag{15}$$

So in total the single-wake model is formulated with respect to $N+2$ d.o.f. for the purely inviscid part $\{\sigma^i, i=1:N\}, \gamma^1, \gamma_W$ and $3\times(N+N_w)$ for the viscous part $\{\delta^{*i}, \theta^i, (\eta^i \text{ or } C_\tau^i)\}$ resulting $\{u_{\tau B}^i, i=1:N\}$. The equations are non-linearly coupled while they implicitly depend on ΔS_w^Δ and θ_w^Δ. The solution of the system is based on the Newton–Raphson algorithm. In every time step, a double iteration loop is defined: given ΔS_w^Δ and θ_w^Δ, the complete set of equations is solved iteratively until convergence is accomplished, then ΔS_w^Δ and θ_w^Δ are corrected and a new iteration loop starts. At the end of each time step, the wake is convected. In this process the near wake segment ΔS_w^Δ is transformed into a vortex blob.

2.4.2. The double-wake model. When the second wake is added, the solution of the boundary layer equations carries on until separation is found on either side of the airfoil (Figure 4). The mass deficit in the separated region leading to reverse flow conditions is obtained through the velocity induced by the vorticity of the separated wake formed over the airfoil in this area. Therefore, downstream of separation $[u_n^*]_B = 0$. The same assumption is also made on the wakes. So $\mathbf{u}^*$ can be merged with $\mathbf{u}^0$ in which case the no-penetration condition (4) changes into

$$(\mathbf{u}_e(\mathbf{x};t) - \mathbf{U}_B(\mathbf{x};t)) \cdot \mathbf{n}(\mathbf{x};t) = \mathbf{w}_e(\mathbf{x};t) \cdot \mathbf{n}(\mathbf{x};t) = \frac{\mathrm{d}M}{\mathrm{d}s} \tag{16}$$

So in total the double-wake model is formulated with respect to $N+4$ d.o.f. for the purely inviscid part $\{\sigma^i, i=1:N\}, \gamma^1, \gamma^2, \gamma_W, \gamma_S$ plus the $3 \times (N_{P_s} - 1)$ d.o.f. for the attached part of the boundary layer. The equations are again non-linearly coupled while they implicitly depend on ΔS_w^Δ, ΔS_s^Δ and θ_w^Δ, θ_s^Δ as well as on the location of separation P_s. Change of P_s requires remeshing on the airfoil, so that P_s is always located at a grid point. In order to maintain reasonable spacing, remeshing is carried out over the entire airfoil surface. Furthermore, update of P_s and remeshing is always done with a converged boundary layer solution.

3. RESULTS AND DISCUSSION

Results are presented for the 17% thick GA(W)-1 airfoil in steady flow conditions and for the NACA0015 and NACA0012 airfoils undergoing pitching motion.

The first case aims at investigating the overall behaviour of the boundary layer modelling especially in stall. This particular case has been chosen because of the quality of the measurements and the availability of pressure data. The quality of the prediction in post stall provides a clear indication also for the quality of the dynamic stall predictions.

The other four sets of results correspond to pitching airfoils, taken from three different measurement campaigns. The following aspects are considered:

(a) Comparison between the single- and double-wake models. This is carried out with respect to a light stall case for the NACA0015.
(b) Validation of the double-wake model in deep stall conditions. This is carried out with respect to two measured cases for the NACA0015 and one for the NACA0012. Validation is performed on the basis of sectional loads. In one of two sets for the NACA0015, pressure data are available which allow a more detailed validation, in particular in relation to the prediction of the separation point.
(c) Investigation of the effect of transition in cases of deep stall. This is done in two cases: one for the NACA0015 and one for the NACA0012.
(d) Investigation of the effect of a laminar bubble over the leading edge which results a massive and abrupt loss of lift followed by moment break. This is done for the NACA0012 which because of its smaller thickness is more sensitive.

3.1. *GA(W)-1 airfoil in steady flow* ($Re = 6.3 \times 10^6, Ma = 0.15$).

The GA(W)-1 airfoil was tested in the NASA Langley low-turbulence pressure tunnel, in free and fixed boundary layer transition [27]. Forced transition is attained using transition strips

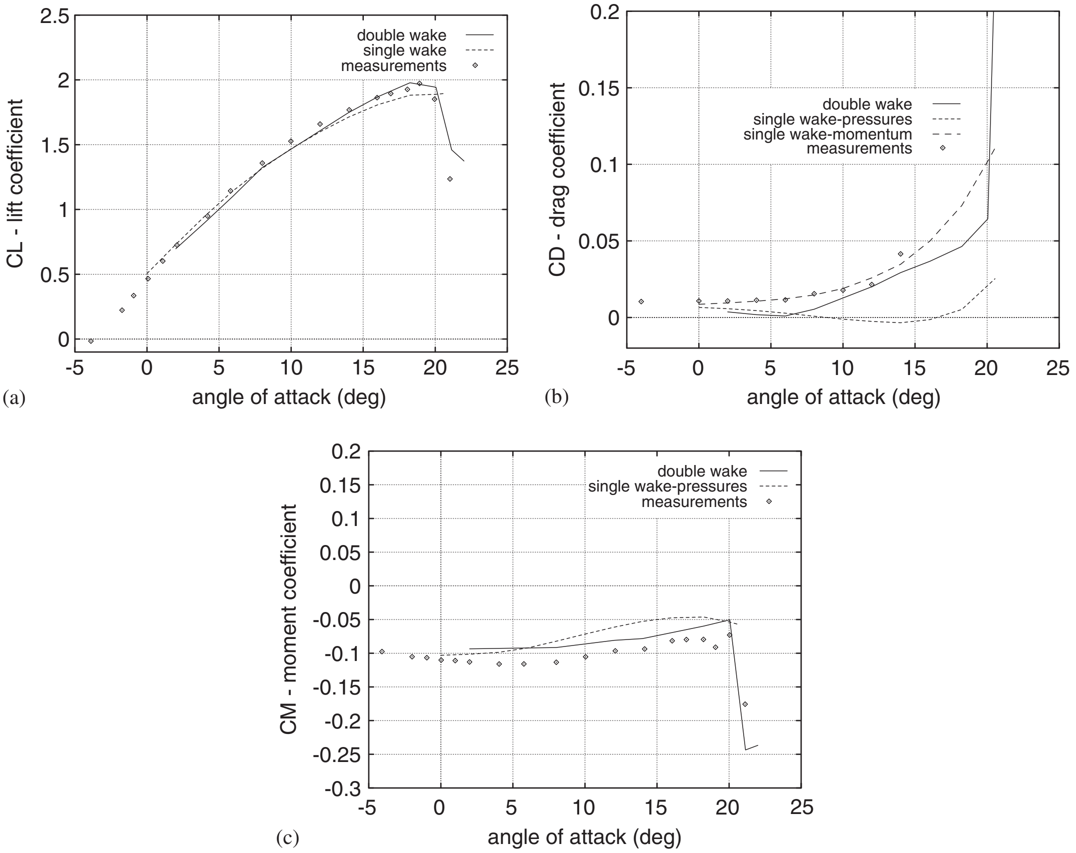

(a) (b) (c)

Figure 5. Aerodynamic loads coefficients *versus* angle of attack for GA(W)-1 in steady state conditions ($Re = 6.3 \times 10^6$, $Ma = 0.15$, transition fixed at 0.08c).

located on both upper and lower surfaces of the airfoil at 8% of the chord. Results are presented, for both models (single and double wake) in tripped flow conditions at $Re = 6.3 \times 10^6$, $Ma = 0.15$.

In Figure 5(a) the predictions for the lift coefficient are compared against measurements. Both models give similar results in the linear part of CL. The double-wake model gives more accurate predictions of CL in the CL_{max} region and provides converged solutions even in the post stall region. The particular airfoil exhibits a very abrupt loss of lift beyond 20° of incidence as a result of the rapid development of separation which moves quickly towards the leading edge within a very short range of incidence. Under such flow conditions, the conventional boundary layer approach (single-wake model) fails to provide converged solution—especially within the separated region. On the contrary, the double-wake model, in which integration of the boundary layer equations is carried out up to the separation point, successfully moves separation very closely to the leading edge at high incidence and predicts the steep drop of the lift. However, the loss of lift seen beyond 20° is less pronounced in the predictions. As discussed later on, this is due to a level difference in the pressure distribution within the separation bubble.

In Figure 5(b), predictions of CD are provided, calculated in two different ways, either by integrating pressure distribution over the airfoil surface or by applying momentum theorem on a control volume surrounding the airfoil. The results obtained using momentum theorem are in much better agreement with measurements as compared to those obtained through integration of local force distributions. Direct pressure integration tends to underestimate drag, especially in the use of the single-wake model, in which case deviations increase as the angle of attack is increasing. This behaviour is due to the inherent weakness of the integral boundary layer methods to provide reliable predictions of the pressure field near and within the separation area. This is due to the suppression of the streamline curvature effects in the integral formulation of the boundary layer equations [28] that become sufficiently large near and beyond separation point in case of separated flows and at the trailing edge point in case of attached flows. The double-wake model gives very similar results with those of the single-wake model up to the incidence of 6° where the flow remains essentially attached. When the flow is attached, the separation point will be lying very closely to the trailing edge and the vorticity shed in the wake will be very low. Thus, modulation of the pressure field strongly depends on the boundary layer solution. As the flow begins to separate the formation of the pressure field inside the separated region is basically regulated by the vorticity distribution over the separated wake sheet. Since this vortex sheet is freely moving, flow curvature effects are properly accounted for and therefore better drag predictions are obtained.

The predictions of the moment coefficient CM are in satisfactory agreement with the measured data (see Figure 5(c)). There is only a slight shift of the predictions as compared to the measurements. As in the case of the lift and the drag, the double-wake model gives again better correlation with the test data.

It is noted that the double-wake model besides converging at much higher angles of attack, it also gives reliable predictions of the aerodynamic loads. This is not only supported by the comparison of the lift coefficient but also by the pressure distributions at the very high incidence of 21.14° in the post stall region (shown in Figure 6). In this case the model predicts well the

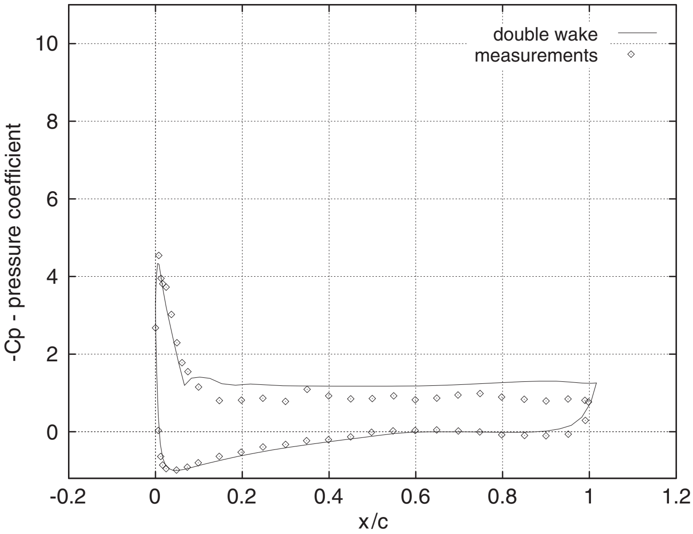

Figure 6. Pressure coefficient distribution for GA(W)-1 at 21.14° angle of attack ($Re = 6.3 \times 10^6$, $Ma = 0.15$, transition fixed at 0.08c).

suction pressure and the location where separation occurs. It slightly underestimates the pressure level inside the separation bubble. At such a high angle of attack, the flow will be unsteady. The two vortex sheets, carrying vorticity of opposite signs, interact strongly with each other and cause the wake to roll up. Thus, successive confined vortex structures of opposite sign are generated in the wake, inducing a harmonic field upstream on the airfoil. In such an unsteady flow case, the pressure distributions and the aerodynamic loads are obtained by averaging over a few periods of this vortex shedding process.

3.2. Pitching NACA0015 ($Re = 2 \times 10^6, Ma = 0.3$)

The NACA0015 airfoil was tested in the U.S. Army subsonic wind tunnel at the NASA Ames Research Center [29]. The conditions of the test included operation both with and without leading edge upper surface boundary layer trip. Boundary layer forced transition was realized using a spanwise row of triangular-shaped pieces located on the upper surface of the wing, at approximately 0.5% of the chord. The conditions of the test were $Re = 2 \times 10^6$ and $Ma = 0.3$.

Predictions are compared against measurements obtained for tripped boundary layer conditions. Two cases are studied corresponding to pitching motion with the same reduced frequency ($k = 0.1$) and amplitude ($\alpha_1 = 4°$) but different mean angles ($\alpha_0 = 11$ and $15°$). The first case corresponds to light stall conditions where the maximum pitching angle ($\alpha_{\max} = 15°$) barely exceeds the static $\mathrm{CL}_{\max}$ angle. The second case is a deep stall case in which the maximum pitching angle reaches $\alpha_{\max} = 19°$.

In Figure 7(a)–(c) results for the lift, drag and moment coefficients are presented for the light stall case. In the same plots the measured steady-state characteristics are also shown. The results are plotted in the form of hysteresis loops, where arrows are used to indicate the direction of the unsteady loops. For this specific case both results from the single- and the double-wake model are shown.

Concerning the lift coefficient Figure 7(a), the double-wake model provides reasonable agreement with measurements. Small deviations are only noted in the reattachment phase, at the end of the downstroke. In simulation fully attached flow is established at 9° while in the measurements reattachment occurs at somehow lower angle (around 8°). The single-wake model provides a less wide dynamic stall loop and higher lift values, as compared to the measurements and the results of the double-wake model. This result is in line with the steady-state lift curve, as predicted by the same model (not shown in the plot).

In the drag coefficient (Figure 7(b)) both models reproduce reasonably well the width and the direction of the loop, with the double-wake model giving slightly better correlation with measurements. As a result of the under-prediction of the drag, already discussed in the previous section, which becomes higher as the incidence increases, the inclination of the loops is miscalculated by both models.

The predicted loops of the moment coefficient (Figure 7(c)) are in fair agreement with measurements except for the beginning of the downstroke where both models over-predict the pitching moment. The direction of the loop is found to be in accordance with measurements.

In Figure 8(a)–(c), the results for the deep stall case are presented. Only predictions from the double-wake model are shown since the single-wake model fails to provide converged solution in such a deep stall case. Two sets of results are provided: the first corresponds to fixed boundary layer transition at 0.5% of the chord, as also done in the tests, while the second corresponds to fixed tripping at the leading edge. This is done so as to investigate the sensitivity of the results

DOI: 10.1002/fld

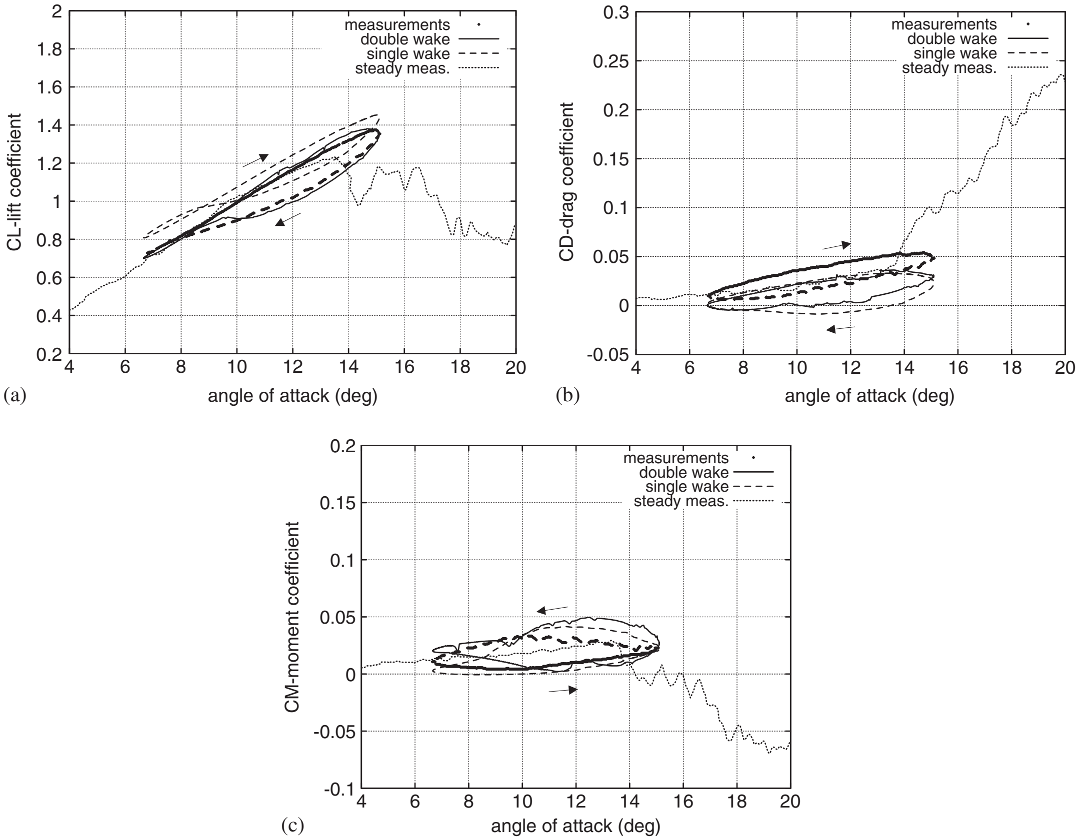

Figure 7. Aerodynamic loads coefficients *versus* angle of attack for a pitching NACA0015 ($Re = 2 \times 10^6$, $Ma = 0.3$, $\alpha_0 = 11°$, $\alpha_1 = 4°$, $k = 0.1$).

to the location of the tripping point. It is noted that specifying a tripping point at 0.5% of the chord allows the code to operate in free transition over the LE starting from the stagnation point. Clearly this will take place at high angles of attack which explains the difference obtained in the predictions. Concerning the lift (Figure 8(a)) satisfactory agreement with measurements is obtained especially when the tripping is placed at 0.5% of the chord. Moving fixed transition to the leading edge leads to a broader dynamic stall loop. Regardless the location of transition, the lift is slightly overestimated during the upstroke.

Also the drag predictions are in good agreement with measurements when transition location matches that of the experiment (Figure 8(b)). The shape and the width of the loop are captured whereas the overshoot of the drag at the maximum pitching angle is slightly exceeded. Fixing transition at the leading edge, as in the case of the lift, provides wider hysteresis loop as compared to measurements.

Results of similar quality are also obtained for the moment coefficient (Figure 8(c)). The negative overshoot of the moment coefficient is well captured when the tripping point is set at 0.5% of the chord. Also the eight-like shape of the loop is consistently reproduced. When tripping location is

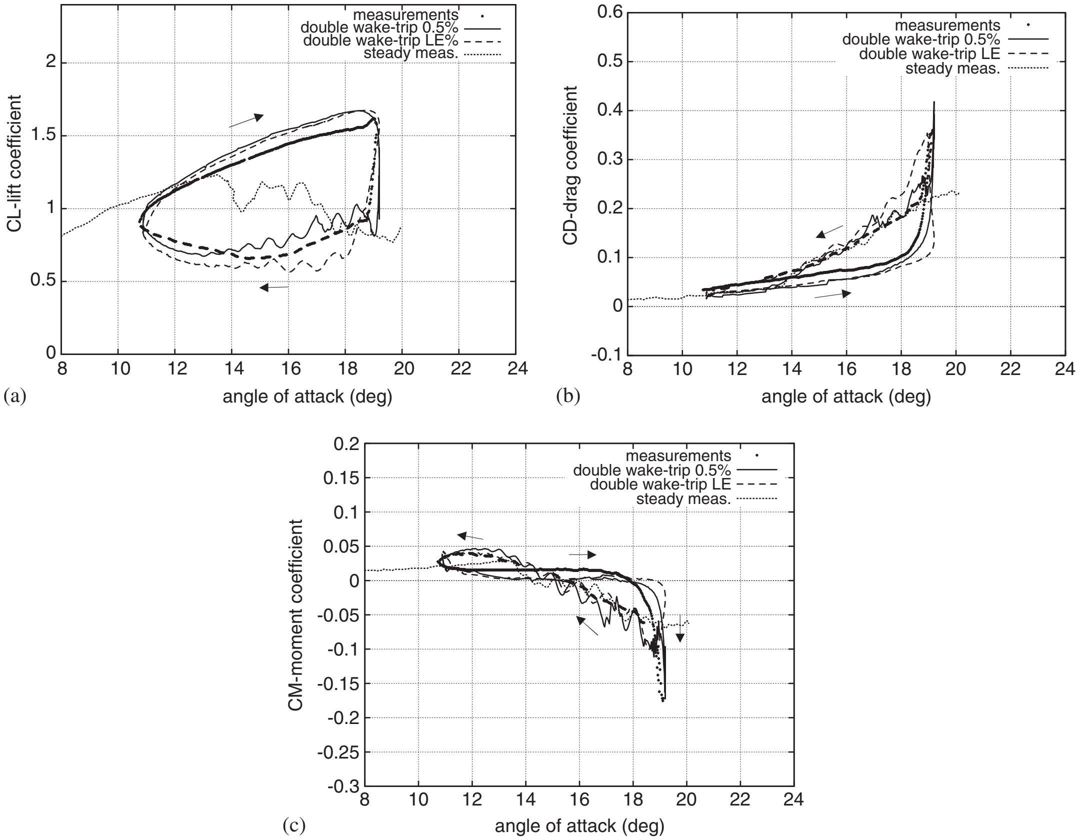

Figure 8. Aerodynamic loads coefficients *versus* angle of attack for a pitching NACA0015 ($Re = 2 \times 10^6$, $Ma = 0.3$, $\alpha_0 = 15°$, $\alpha_1 = 4°$, $k = 0.1$).

placed at the leading edge of the airfoil, the predicted overshoot is found to be less pronounced. However, even in this case the shape of the predicted loop follows quite closely the measurements.

It is noted that in all aerodynamic loads a high-frequency oscillation is observed during the downstroke which is not present in the measurements. This is due to the unsteady vortex shedding of successive counter-sign vortex structures in the wake, which takes place in cases of massive flow separation, and results from the strong interaction of the trailing and separated vortex sheets (Figure 9). Due to the absence of any diffusion in the wake modelling, these vortex structures remain confined and therefore they are expected to induce an oscillatory effect on the pressure field on the airfoil.

3.3. Pitching NACA0015 ($Re = 1.5 \times 10^6, Ma = 0.12$).

In this section results are presented again for a NACA0015 undergoing oscillatory motion from a different test campaign. Predictions are compared to measurements conducted in Glasgow University low-speed wind tunnel [30] at $Re = 1.5 \times 10^6$ and $Ma = 0.12$. A deep stall case is

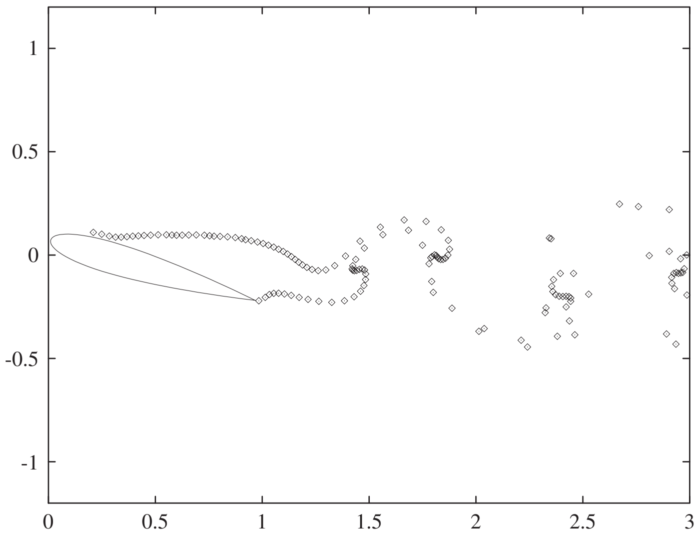

Figure 9. Unsteady vortex shedding during airfoil's downstroke.

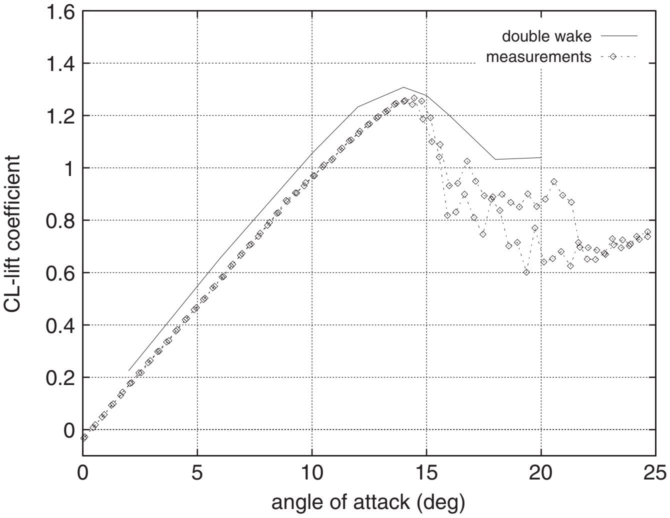

Figure 10. Lift curve for a NACA0015 in steady-state flow ($Re = 1.5 \times 10^6$, $Ma = 0.12$).

studied, corresponding to pitching motion with mean angle $\alpha_0 = 11°$, amplitude $\alpha_1 = 8°$ and reduced frequency $k = 0.05$. The maximum angle over the oscillation cycle ($\alpha_{\max} = 19°$) of this particular case is far beyond the static $\text{CL}_{\max}$ angle which for the specific airfoil and the specific flow conditions is about 14° (Figure 10). In the CL measurements shown in Figure 10, there is a slight shift of the zero-lift angle of attack together with a deviation in slope as compared to predictions. They suggest the presence of 3D effects in the measurements.

DOI: 10.1002/fld

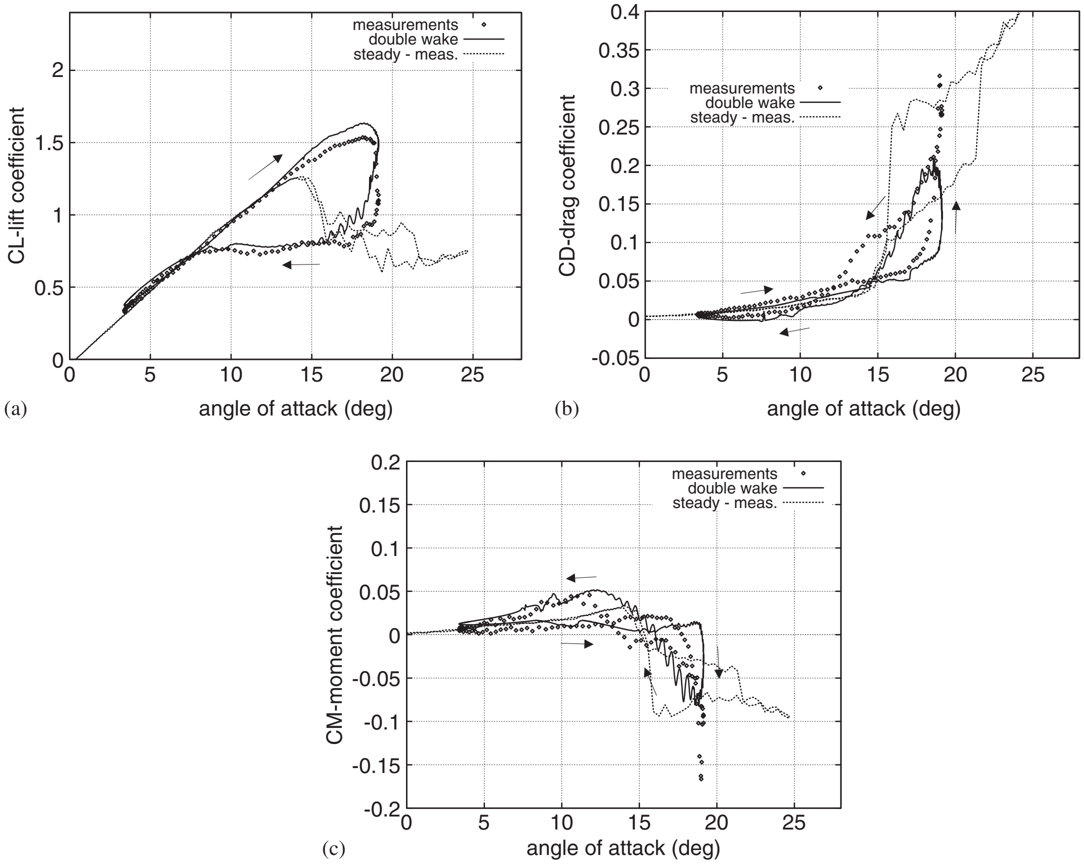

Figure 11. Aerodynamic loads coefficients *versus* angle of attack for a pitching NACA0015 ($Re = 1.5 \times 10^6$, $Ma = 0.12$, $\alpha_0 = 11^\circ$, $\alpha_1 = 8^\circ$, $k = 0.05$).

In Figure 11(a)–(c) the aerodynamic loads *versus* the pitching angle are shown over the cycle of oscillation. In the same figures, along with the unsteady load coefficients, the steady-state measured curves of the lift, drag and moment coefficients are also presented. It is noted that the steady-state measurements are given in loop form, as done with the unsteady results. This is because in the measurement campaign, the steady-state conditions were represented by means of a very slow ramp up and down motion of the airfoil. As expected, the effect of the unsteadiness of the flow is more evident in the post stall region where the flow about the airfoil will be unsteady even if the airfoil is still. As in the previous section only double-wake model results are shown.

The maximum value of the lift is slightly overestimated while small deviations in the shape of the CL loop are noted in the region close to the maximum pitching angle, especially when the airfoil begins to move downwards (Figure 11(a)). Looking into the predicted unsteady pressure distributions (Figure 12), it is noted that the maximum extent of separation and therefore the loss of the lift occur when the airfoil begins its downstroke. In the measurements the separation point

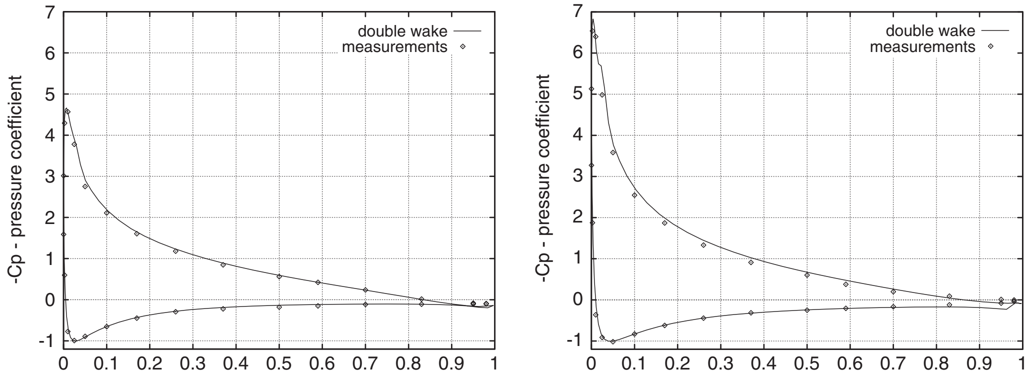

(a) upstroke 12°

(b) upstroke 15°

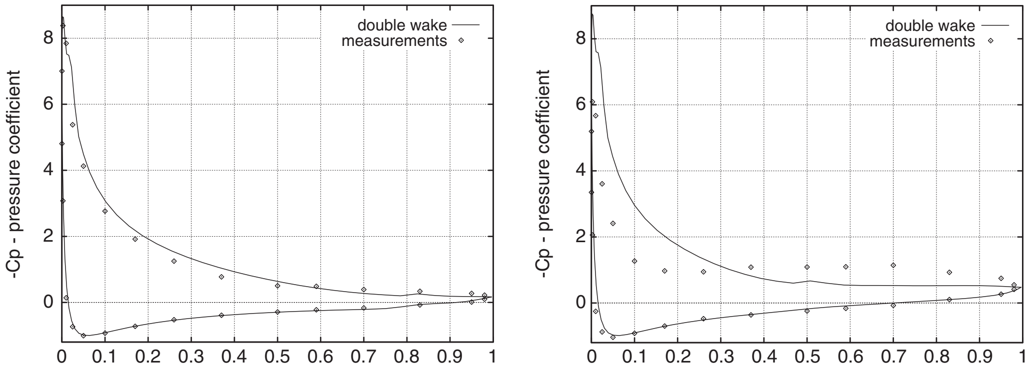

(c) upstroke 18°

(d) upstroke 19°

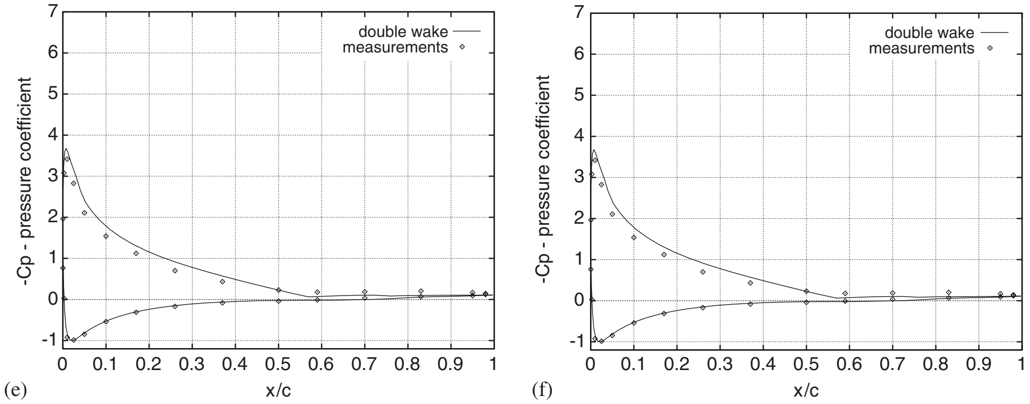

(e) downstroke 12°

(f) downstroke 15°

Figure 12. Pressure coefficient distribution of a pitching NACA0015 at different pitching angles ($Re = 1.5 \times 10^6$, $Ma = 0.12$, $\alpha_0 = 11°$, $\alpha_1 = 8°$, $k = 0.05$).

DOI: 10.1002/fld

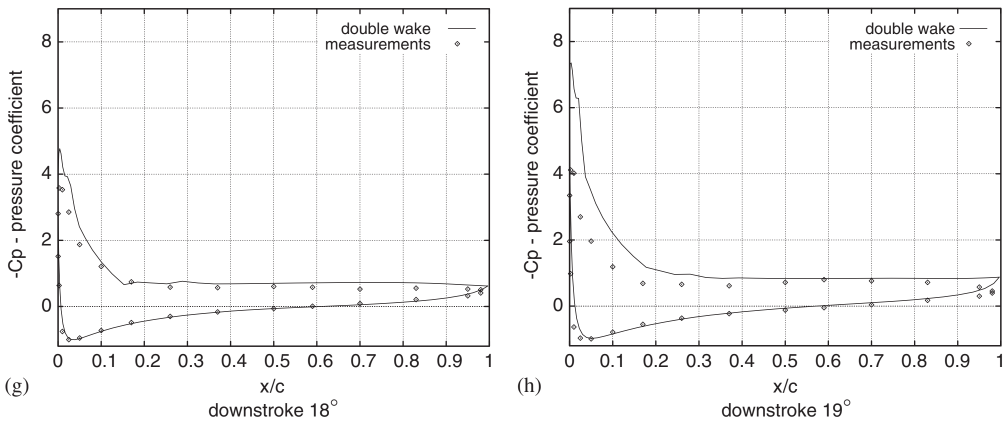

Figure 12. *Continued.*

approaches the leading edge region (Figure 12(d)) before the airfoil reaches the maximum angle. The above differences are found to be in close connection with the different post stall behaviour noted for steady-state conditions. In Figure 10 it is clearly seen that predictions give a higher CL_{max} value and a delayed loss of lift with respect to the measurements.

Concerning the drag coefficient (Figure 11(b)), the model consistently predicts the shape of the loop. The maximum value of drag is underestimated but in accordance with the measurements it is obtained at the maximum pitching angle. The predicted values of drag are significantly below measurements, throughout the downstroke. A better correlation is obtained in the upstroke except for the part near the maximum angle.

For the moment coefficient (Figure 11(c)) the model fails again to predict the overshoot in the onset of dynamic stall. As already seen in the previous example, such an overshoot is connected to the onset of transition at the LE. By allowing free transition in the previous example such an overshoot was obtained. A similar analysis could be conducted for this case as well. However, because of the doubts concerning 3D effects in the measurements, it was considered better to consider this issue in the case of the NACA0012. Otherwise, the agreement with measurements in the rest of the cycle is reasonably good.

In Figure 12 the surface pressure coefficient distributions at various pitching angles are shown. It is noted that during the upstroke and up to 18° (Figure 12(a)–(c)) a good agreement between predictions and measurements is obtained. Over this part the flow remains practically attached. In the experiment, at 19° of the upstroke, the flow appears fully separated (Figure 12(d)). The separation point moves quickly upstream to the 15% chordwise position, within a range of 1° of the pitch-up motion, and remains there until the 18° of the pitch-down motion. In the calculations and at the angle of 19° (upstroke), the separation point has not yet reached the nearest to leading edge position. This happens at 18° of the downstroke. For this angle (Figure 12(g)), the agreement between predictions and measurements is fair. The chordwise location of separation is captured while the suction pressure is slightly overestimated. Similar results are obtained in the rest of the downstroke (Figure 12(e) and (f)). The model reproduces well the downstream movement of the separation point towards the trailing edge during the reattachment process.

3.4. *Pitching NACA0012* ($Re = 4\times 10^6, Ma = 0.3$)

In the present section results are presented for a pitching NACA0012. Predictions are compared to measurements performed by McCroskey *et al.* [31] for an oscillatory motion with a mean angle and amplitude of 10° and a reduced frequency of $k = 0.05$ at $Re = 4\times 10^6$ and $Ma = 0.3$. The particularity of the 12% thickness airfoil as compared to the 15% thickness airfoil examined in the previous sections is that even when the boundary layer is tripped very close to the leading edge, a strong laminar separation bubble is formed right after the stagnation point even at moderate incidence. In the presence of this laminar bubble, full separation of the boundary layer can be initiated during the upstroke or at the beginning of the downstroke with a direct effect on the dynamic stall characteristics of the airfoil, as indicated in [32].

In Figure 13 predictions of the normal force CN, drag CD and moment CM coefficients for tripped and free transition conditions are compared to the experimental data. As indicated in Figure 14, where the hysteresis loop of the separation location is shown, before the airfoil reaches the maximum angle, separation moves fast towards the leading edge within a very short range of incidence. In the calculation this shift occurs in a couple of time steps of the numerical computation

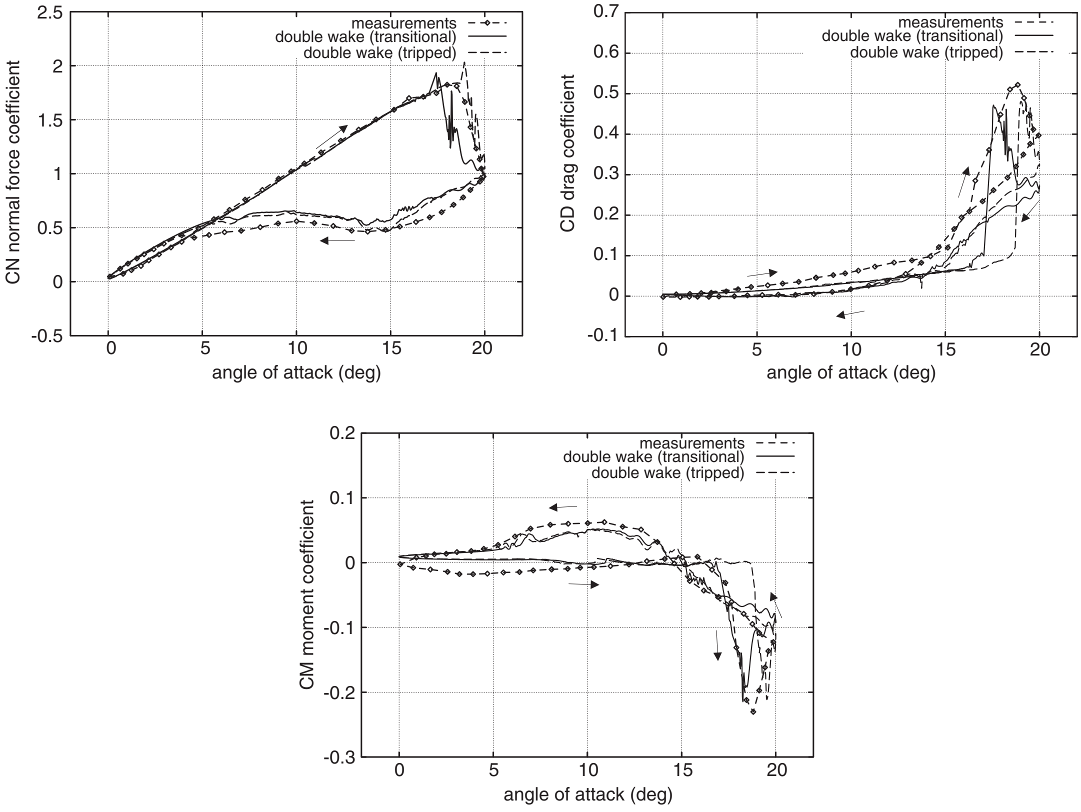

Figure 13. Aerodynamic loads coefficients *versus* angle of attack for a pitching NACA0012 ($Re = 4\times 10^6$, $Ma = 0.3$, $\alpha_0 = 10°$, $\alpha_1 = 10°$, $k = 0.05$).

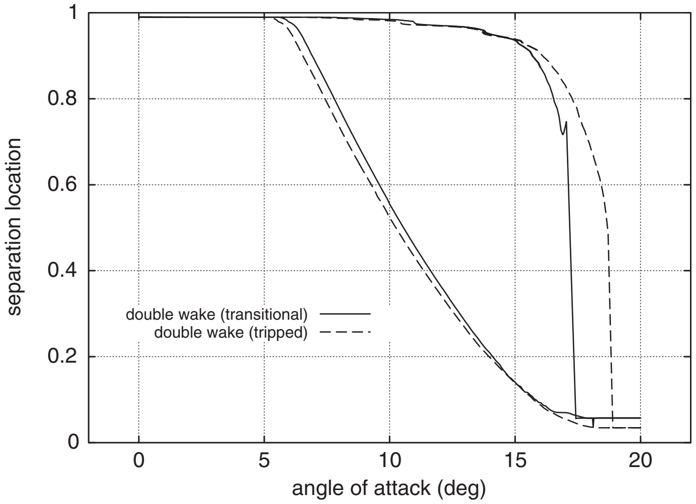

Figure 14. Hysteresis loop of separation location for a pitching NACA0012 ($Re = 4 \times 10^6$, $Ma = 0.3$, $\alpha_0 = 10°$, $\alpha_1 = 10°$, $k = 0.05$).

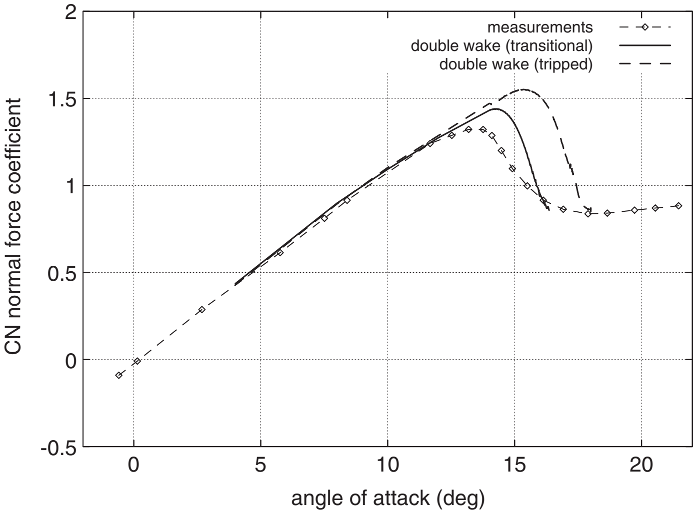

Figure 15. Normal force coefficient curve for a NACA0012 in steady-state flow ($Re = 4 \times 10^6$, $Ma = 0.3$).

and it is closely linked to the development and evolution of the laminar separation at the leading edge. In case of free transition the loss of lift occurs earlier as a result of the larger extend of the leading edge bubble. This is also supported by the steady-state results presented in Figure 15. In the free transition computation, the maximum CN as well as the angle that the maximum CN is obtained are lower. In both computations when separation moves at the leading edge a local

DOI: 10.1002/fld

increase in CN is obtained, resulting from the vortical structure that is formed by the free vorticity suddenly released from near the leading edge point, travelling over the suction side of the airfoil. The spiky behaviour noted right after this localized increase in CN is associated with the relatively large time step used, compared to the time scale of the phenomenon in this part of the cycle. It is noted that a constant time step is used throughout the computation. In the prediction of CD, the method under-predicts drag as also noted in previous examples but it reproduces correctly the shape of the hysteresis loop. In CM a good agreement is obtained both in terms of the shape of the loop and also the value of CM at the onset of dynamic stall especially in the case of the transitional computation.

4. CONCLUSIONS

A dynamic stall model for pitching airfoils has been presented on the basis of the double-wake concept in the context of strong viscous–inviscid interaction boundary layer theory. Validation against existing wind tunnel measurements shows that the model is capable of performing unsteady simulations on pitching airfoils with good accuracy even in deep stall conditions. Despite its simplicity in comparison to CFD models [6], consistent predictions of the loads both integrated and distributed have been obtained.

The introduction of the separated vortex sheet proved to be crucial in obtaining converged solutions even for massively separated flow conditions, as opposed to standard boundary layer formulations that usually fail to handle large flow separations. Also important is the ability of the model to handle transition. By allowing free transition in agreement with the test conditions, predictions were significantly improved. Furthermore in case the laminar separation bubble at the LE is strong enough, the model will predict the onset of massive separation seen in the measurements.

From an engineering point of view, the low computational cost of the model is a clear advantage of the proposed model and therefore it is very attractive for engineering applications and in particular those dealing with aeroelastic simulations. More specifically for a pitching airfoil in deep stall, convergence to a periodic solution is obtained in an hour on a single PC processor while on the same processor a RANS solver with adequate resolution would require more than a day.

ACKNOWLEDGEMENTS

The authors are sincerely grateful to Professor Mark Drela for his help during the course of this work. Without his help, it would have been impossible to proceed with the work presented herein.

NOMENCLATURE

$\mathbf{u}$	absolute velocity
$\mathbf{w}$	relative velocity
$\mathbf{U}_\infty$	velocity at infinity
S	surface
Φ	potential of the flow
$\mathbf{n}$	normal unit vector
$\boldsymbol{\tau}$	tangent unit vector

$\mathbf{k}$	unit vector normal to the plane of the flow
Δh	pressure difference between the separation bubble and the outer flow
[ ]	jump across a line
L_1	length of the attached part of the flow on the airfoil
L_2	length of the separated part of the flow on the airfoil
$\mathbf{x}, \mathbf{y}$	position vectors
$\mathbf{r}$	distance between two points $\mathbf{r}=\mathbf{x}-\mathbf{y}$, $r=\lvert\mathbf{r}\rvert$
σ	source intensity
γ	surface vorticity intensity
$\boldsymbol{\Gamma}$	vortex blob intensity
$\mathbf{Z}$	vortex blob position
t	time
N	number of panels on the airfoil
N_W	number of panels on the trailing edge wake
N_{P_s}	separation point node
N_{P_s}	separation point location
ΔS	length of a panel
Δt	time step
θ^{Δ}	orientation of near wake panels
δ	the boundary layer thickness
δ^*	the displacement thickness $\int_0^\delta (1-(\rho u/\rho_e u_e))\,\mathrm{d}\eta$
δ^{**}	density thickness $\int_0^\delta (u/u_e)(1-(\rho/\rho_e))\,\mathrm{d}\eta$
θ	the momentum thickness $\int_0^\delta (\rho u/\rho_e u_e)(1-(u/u_e))\,\mathrm{d}\eta$
θ^*	kinetic energy thickness $\int_0^\delta (\rho u/\rho_e u_e)(1-(u^2/u_e^2))\,\mathrm{d}\eta$
H	shape parameter δ^*/θ
H^*	kinetic energy shape parameter θ^*/θ
H^{**}	density shape parameter δ^{**}/θ
Θ_n	momentum transport in the normal direction $1/(\rho_e u_e^2)\int_0^\delta (\rho_e u_e v_e - \rho u v)\,\mathrm{d}\eta$
C_f	skin friction coefficient $2\tau_{wall}/(\rho_e u_e^2)$
C_τ	shear stress coefficient $\tau_{\max}/(\rho_e u_e^2)$
C_D	dissipation coefficient $1/(\rho_e u_e^3)\int_0^\delta \tau(\partial u/\partial\eta)\,\mathrm{d}\eta$
Ω	angular velocity
a	local flow acceleration
ρ	density
$D_{I,i}$	finite difference operator
k	reduced frequency $\Omega\cdot c/(2\cdot U_\infty)$
CL	lift coefficient
CN	normal force coefficient
CD	drag coefficient
CM	moment coefficient

Superscripts, subscripts

e	refers to the 'equivalent inviscid flow' field (EIF)
$*$	refers to the viscous correction of the flow

0	refers to the purely inviscid part of the flow
B	refers to the airfoil
W	refers to the trailing edge wake
S	refers to the separation wake
n	denotes the normal component
τ	denotes the tangential component
i	refers to panel center
I	refers to grid node
1	refers to the attached part of the flow on the airfoil
2	refers to the separated part of the flow on the airfoil
Δ	refers to the wake panels generated during the current time step
u, ℓ	refers to the two sides of the trailing edge wake

REFERENCES

1. Ekaterinaris JA, Platzer MF. Computational prediction of airfoil dynamic stall. *Progress in Aerospace Sciences* 1998; **33**:759–846.
2. Petot D, Szechenyi E, Arnaud G, Harrison R, Stevens J, Teves D, van der Wall B, Young C. Stall effects and blade torsion—an evaluation of predictive tools. *23rd European Rotorcraft Forum*, Dresden, Germany, 1997; Paper 32.
3. Snel H. Review of the present status of rotor aerodynamics. *Wind Energy* 1998; **1**:46–69.
4. Leishman JG, Beddoes TS. A generalized model for airfoil unsteady aerodynamics behavior and dynamic stall using indicial method. *Proceedings of the 42nd Annual Forum of the American Helicopter Society*, Washington, DC, 1986; 243–265.
5. Petot D. Differential equation modeling of dynamic stall. *La Recherche Aerospatiale* (English Edition) 1989; **5**:59–72.
6. Ekaterinaris JA, Srinivasan GR, McCroskey WJ. Present capabilities of predicting 2D Dynamic-Stall. *AGARD-CP-552 Proceedings of the Aerodynamics and Aeroacoustics of Rotorcraft*, Berlin, 1995; Paper 2.
7. Hald O. Convergence of vortex methods II. *SIAM Journal of Numerical Analysis* 1979; **16**:726–755.
8. Beale JT, Majda A. Vortex methods II: High order accuracy in 2 and 3 dimensions. *Mathematics of Computation* 1982; **32**:29–52.
9. Koumoutsakos P, Leonard A. High resolution simulations of the flow around an impulsively started cylinder using vortex methods. *Journal of Fluid Mechanics* 1995; **296**:1–38.
10. Voutsinas SG, Riziotis VA. Vortex particle modeling of stall on rotors. Application to wind turbines. *Proceedings of the Fluids Engineering Division Summer Meeting*, ASME, San Diego, 1996.
11. Basu BC, Hancock GJ. The unsteady notion of a two-dimensional airfoil in incompressible, inviscid flow. *Journal of Fluid Mechanics* 1978; **87**(Part 1):159–178.
12. Katz J. A discrete vortex method for the non-steady separated flow over an airfoil. *Journal of Fluid Mechanics* 1981; **102**:315–328.
13. Vezza M, Galbraith RAMcD. An inviscid model of unsteady aerofoil flow with fixed upper surface separation. *Journal for Numerical Methods in Fluids* 1985; **5**:577–592.
14. Maskew B, Dvorak FA. The prediction of $\mathrm{CL}_{\mathrm{max}}$ using a separated flow model. *Journal of American Helicopter Society* 1977; **23**(2):2–8.
15. Kermarec M, Decaix AF, Renon P, Favier D, Maresca C. Numerical modeling of unsteady flows around airfoils by a coupled potential-boundary-layer method. *European Journal of Mechanics*, *B-Fluids* 1993; **12**(5):657–681.
16. Voutsinas SG, Riziotis VA. A viscous–inviscid interaction model for dynamic stall simulations on airfoils. *AIAA*, 1999; Paper 99-0038.
17. Drela M. XFOIL: an analysis and design system for low Reynolds number airfoils. *Conference on Low Reynolds Number Aerodynamics*, University Notre Dame, 1989.
18. Drela M, Giles M. Viscous–inviscid analysis of transonic and low Reynolds number airfoils. *AIAA Journal* 1987; **25**(10):1347–1355.

19. Lock RC, Williams BR. Viscous–inviscid interactions in external aerodynamics. *Progress in Aerospace Science* 1987; **24**:51–171.
20. LeBalleur JC. Strong matching method for computing transonic viscous flows including wakes and separations. Lifting airfoils. *Rec. Aerospatiale No. 1981-3*, 1981.
21. Cebeci T (ed.). *Numerical and Physical Aspects of Aerodynamic Flows* (vol. IV). Springer: Berlin, 1990.
22. Morino L, Kuot C-C. Subsonic potential aerodynamics for complex configurations: a general theory. *AIAA Journal* 1974; **12**(2):191–197.
23. Swafford TW. Analytical approximation of two-dimensional separated turbulent boundary-layer velocity profiles. *Journal AIAA* 1983; **21**(6):923–926. Technical notes.
24. van Ingen JL. A suggested semi-empirical method for the calculation of the boundary layer transition region. *Report VTH-74*, Department of Aerospace Engineering, Delft University of Technology, 1956.
25. Green JE, Weeks DJ, Brooman JWF. Prediction of turbulent boundary layers and wakes in compressible flow by a Lag-Entrainment method. *ARC R&M Report No. 3791*, HMSO, London, England, 1977.
26. Bradshaw P, Ferriss DH. Calculation of boundary layer development using the turbulent energy equation: compressible flow on adiabatic walls. *Journal of Fluid Mechanics* 1970; **46**(Part 1):83–110.
27. McGhee RJ, Beasley WD. Low speed aerodynamic characteristics of a 17-percent-thick airfoil section designed for general aviation applications. *NASA TN D-7428*, 1973.
28. East LF. A representation of second order boundary layer effects in the momentum integral equation and in viscous–inviscid interactions. *RAE Technical Report*, 1981.
29. Piziali RA. An experimental investigation of 2D and 3D oscillating wing aerodynamics for a range of angles of attack including stall. *NASA Technical Memorandum 4632*, 1994.
30. Galbraith RAMcD, Gracey MW, Leitch E. Summary of pressure data for thirteen aerofoils on the University of Glasgows aerofoil data base. *G.U. Aero Report 9221*, 1992.
31. McCroskey WJ, McAlister KW, Carr LW, Pucci SL. An experimental study of dynamic stall on advanced airfoil sections. *NASA TM-84245* (vols 1, 2 and 3), 1982.
32. Ekaterinaris JA, Platzer MF. Numerical investigation of stall flutter. *Journal of Turbomachinery* (ASME) 1996; **118**:197–203.

DOI: 10.1002/fld